Electronic Seismologist

# gCAPjoint, A Software Package for Full Moment Tensor Inversion of Moderately Strong Earthquakes with Local and Teleseismic Waveforms

Qipeng Bai[1], Sidao Ni[*2], Risheng Chu[2], and Zhe Jia[3]

## Abstract

**Earthquake moment tensors and focal depths are crucial to assessing seismic hazards and studying active tectonic and volcanic processes. Although less powerful than strong earthquakes (M 7+), moderately strong earthquakes (M 5–6.5) occur more frequently and extensively, which can cause severe damages in populated areas. The inversion of moment tensors is usually affected by insufficient local waveform data (epicentral distance < 5°) in sparse seismic networks. It would be necessary to combine local and teleseismic data (epicentral distance 30°–90°) for a joint inversion. In this study, we present the generalized cut-and-paste joint (gCAPjoint) algorithm to jointly invert full moment tensor and centroid depth with local and teleseismic broadband waveforms. To demonstrate the effectiveness and explore the limitations of this algorithm, we perform case studies on three earthquakes with different tectonic settings and source properties. Comparison of our results with global centroid moment tensor and other catalog solutions illustrates that both non-double-couple compositions of the focal mechanisms and centroid depths can be reliably recovered for very shallow (< 10 km) earthquakes and intermediate-depth events with this software package.**

**Cite this article as** Bai, Q., S. Ni, R. Chu, and Z. Jia (2020). gCAPjoint, A Software Package for Full Moment Tensor Inversion of Moderately Strong Earthquakes with Local and Teleseismic Waveforms, *Seismol. Res. Lett.* **91**, 3550–3562, doi: 10.1785/0220200031.

**Supplemental Material**

## Introduction

Accurate earthquake source parameters (e.g., magnitude, focal depth, and moment tensor) are fundamental information for studies of active tectonic and volcanic processes and seismic hazard assessment. Compared with strong earthquakes (**M** 7+), moderately strong earthquakes (**M** 5.0–6.5) can sometimes cause substantial damages in populated areas, because they are more abundant in the interplate and intraplate settings (Baumbach *et al.*, 1994; Hamzehloo, 2005), for example, the 1998 $M_w$ 5.7 Zhangbei-Shangyi (China) earthquake (Li *et al.*, 2008), the 2017 $M_w$ 5.0 Muji-Tashkorgan (India) earthquake (Li *et al.*, 2018), and the 2009 $M_w$ 5.9 L'Aquila (Italy) earthquake (Herrmann *et al.*, 2011). The L'Aquila event has caused a total of 299 reported fatalities, and 1500 injuries resulted from building collapses, and 64,812 people were displaced from their homes (Akinci and Malagnini, 2009). Moreover, some moderately strong earthquakes occur in areas of low historical seismicity, and their source parameters may provide valuable information for seismotectonic studies (Chen *et al.*, 2015). Therefore, it is important to develop algorithms and software packages to retrieve reliable source parameters for moderately strong earthquakes.

Researchers have developed many methods to invert for earthquake source parameters. These methods use broadband seismic waveforms to obtain the source parameters using either waveform fitting in the time domain (Dziewonski *et al.*, 1981; Kanamori, 1993; Dreger and Woods, 2002; Sokos and Zahradnik, 2008; Adamova *et al.*, 2009), or amplitude spectra in the frequency domain (Cesca *et al.*, 2006; Herrmann *et al.*, 2011), or a hybrid approach in the time-frequency domain (Vavryčuk and Kühn, 2012). Among these approaches, the global centroid moment tensor (Global CMT) method and the

1. School of Earth and Space Sciences, University of Science and Technology of China, Hefei, China; 2. State Key Laboratory of Geodesy and Earth's Dynamics, Innovation Academy for Precision Measurement Science and Technology, Chinese Academy of Sciences, Wuhan, China; 3. Seismological Laboratory, California Institute of Technology, Pasadena, California, U.S.A.

*Corresponding author: sdni@whigg.ac.cn

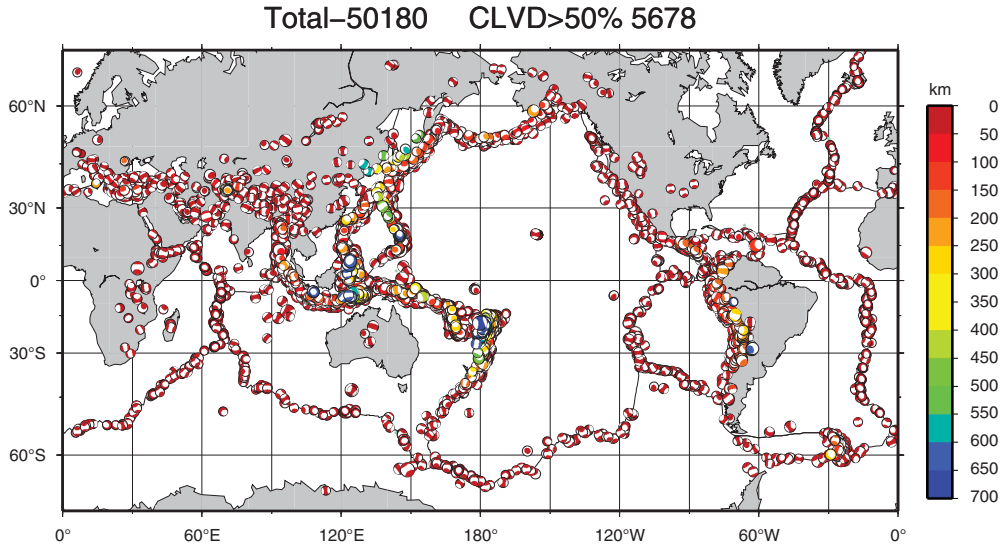


**Figure 1.** Moment tensors (displayed as focal sphere) and focal depths from the Global Centroid Moment Tensor (CMT) catalog for earthquakes from 1 January 1976 to 18 April 2019.

*W*-phase method are the most commonly used (Dziewonski *et al.*, 1981; Kanamori, 1993). The Global CMT tries to fit intermediate-period body waves, long-period surface waves, and very long-period surface waves to constrain the source parameters. It is very stable as long-period filtering (e.g., $T > 40$ s) suppresses the effects of structure heterogeneities. Therefore, the Global CMT solutions are extensively applied in tectonics and seismological studies. The *W*-phase method uses the long-period *W* phases with a period of 100–1000 s between the *P* and *S* waves, and can obtain reliable earthquake source parameters. However, due to the long-period waveforms, the Global CMT and *W*-phase methods might provide limited constraint on focal depths for very shallow earthquakes. For example, their centroid depths have a minimum value of 12 km (Duputel *et al.*, 2012; Ekström *et al.*, 2012).

Instead, earthquake centroid depths can be better resolved with seismic waveform data of shorter periods (a few to dozens of seconds) at local or regional distances. The time domain seismic moment tensor inversion (TDMT_INV) method has been used to study various types of earthquakes (tectonic, volcanic, and explosions) with **M** 2–8 (Dreger and Helmberger, 1993; Minson and Dreger, 2008; D'Amico, 2018). Herrmann and Ammon (1997) also developed a waveform inversion method for **M** > 3 earthquakes. To suppress the effects of lateral variation in the crustal structures, Zhao and Helmberger (1991) introduced the cut-and-paste method (CAP). Within the CAP algorithm, local seismic waveforms are partitioned into *Pnl* and surface-wave segments, which are allowed to shift independently to account for inaccurate velocity structures. Usually, surface waves are much stronger than the *Pnl* waves, because the former decays approximately as $r^{0.5}$ (in which *r* is the distance) and the latter decays as $r^{1}$. To balance their contribution in the waveform inversion, the *Pnl* and surface waves are assigned with different weights to overcome the biases due to the very different amplitudes of these two types of waves. For the case of very sparse local network, Chen *et al.* (2015) developed a CAPjoint algorithm, which combines three-component local waveforms (for epicentral distance within a few 100 km) and teleseismic body waves (for epicentral distance of 30°–90°) for joint inversion of earthquake source parameters. The joint inversion algorithm utilizes more depth phases and provides better distance and azimuthal coverage with a global seismic network. Thus, it achieves more reliable inversion of centroid depths and focal mechanisms for moderately strong earthquakes.

The CAPjoint method assumes double-couple (DC) focal mechanisms, which might work well for most tectonic earthquakes. However, previous studies have shown that some earthquakes can have non-double-couple (non-DC) components (Julian, 1983; Julian and Sipkin, 1985; Frohlich, 1994; Tape and Tape, 2013), especially for earthquakes rupturing along nonplanar faults, collapse of a cavity in mines, fluid injection in geothermal or volcanic regions, and strong seismic anisotropy near the hypocenter (Julian *et al.*, 1998; Miller *et al.*, 1998; Templeton and Dreger, 2006; Ford *et al.*, 2008; Minson and Dreger, 2008; Vavryčuk *et al.*, 2008; Guilhem *et al.*, 2014). The Global CMT catalog between 1976 and 2019 shows that about 10% of the earthquakes have compensated linear vector dipole (CLVD) components >50% in the moment tensors (Fig. 1). Therefore, the CAPjoint method needs to be improved for full moment tensor inversions.

Recently, Zhu and Ben-Zion (2013) extended the classic CAP algorithm to generalized cut-and-paste (gCAP), which can invert full moment tensors with local seismic waveforms. In this article, we combine the gCAP and the CAPjoint algorithm to establish a joint inversion package (generalized cut-and-paste joint [gCAPjoint]), which takes advantage of both local and teleseismic waveforms (the manual is provided in the supplemental material, and the software package is available in Data and Resources). Robustness of this method is demonstrated with case studies of three earthquakes in different tectonic regions and different depths.

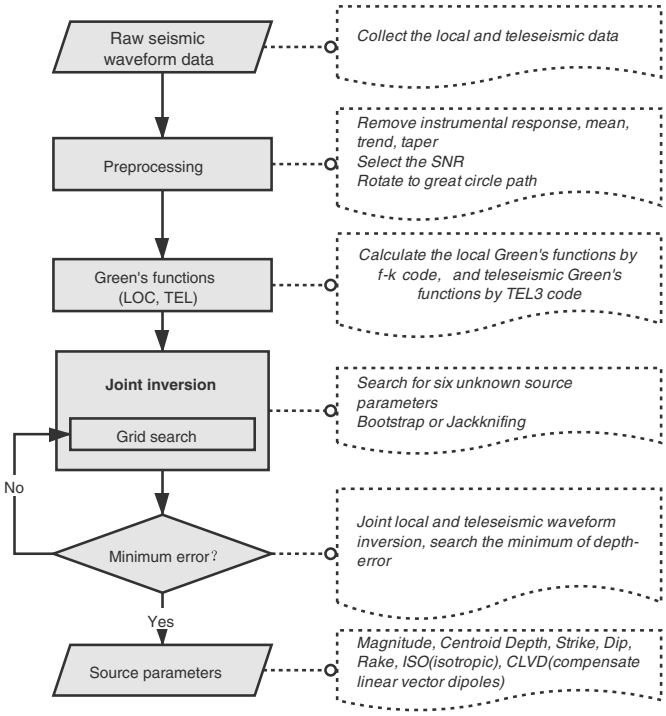


**Figure 2.** Flow chart for the generalized cut-and-paste joint (gCAPjoint) package. Frequency–wavenumber integral method (*f*-*k*) and teleseismic body-wave synthetic code (TEL3) are tools for computing Green's functions at local and teleseismic distances, respectively. CLVD, compensated linear vector dipole; ISO, isotropic; SNR, signal-to-noise ratio.

## The Joint Inversion Algorithm gCAPjoint

Following the CAPjoint method (Chen *et al.*, 2015), the procedures of our gCAPjoint inversion are displayed in Figure 2. This software package adopts the waveform inversion method to determine the full moment tensor and centroid depth. Before the waveform inversion, we calculate the synthetic waveforms that depend on the source parameters and process the observed raw waveform data to obtain ground displacement seismograms. Thereafter, the optimal moment tensor is found via minimizing the error between observed and synthetic waveforms as follows:

$$e = ||u(t) - s(t - \Delta t)||^2, \tag{1}$$

in which $u(t)$ and $s(t)$ are the observed and synthetic waveforms, respectively; $\Delta t$ is the time shift due to the error in the earthquake location or the imperfect velocity model structure. Then the optimal centroid depth could be determined by grid searching different depths.

Synthetic waveforms are calculated with Green's functions at both local and teleseismic distances. The local Green's functions are obtained by a frequency–wavenumber (*f*-*k*) method (Zhu and Rivera, 2002) for a local 1D velocity model. The teleseismic Green's functions are calculated with the propagation matrix method (the TELESEIS package) (Kikuchi and Kanamori, 1982; Chu *et al.*, 2014), and two 1D layered models are allowed for the source side and receiver side, respectively. The TELESEIS package is modified so that it generates Green's functions in the same format as the *f*-*k* package, and we name the new package as TEL3 (teleseismic body-wave synthetic code). Calculation of teleseismic Green's functions requires parameters of mantle attenuation for both *P* and *SH* waves (the $t^*$). In this study, $t^*$ for *P* is set to be 1.0 s and that for *SH* is 4.0 s (Langston, 1978). During the calculation of Green's functions, the crust2.0 model is usually adopted (Bassin, 2000), unless more accurate crustal velocity model is available. IASPEI91 model (Kennett and Engdahl, 1991) was used as the 1D mantle velocity structure for deep earthquakes (focal depth > 30 km). Other models such as AK135 model (Kennett, 2005) or PREM model (Dziewonski and Anderson, 1981) could also be adopted.

Synthetic seismograms can be obtained with linear combination of solutions from four basic source mechanisms: a dip-slip fault with a dipping angle of 45° (DD), a vertical dip-slip fault (DS), a vertical strike-slip fault (SS), and pure isotropic (ISO) components (EP) (Minson and Dreger, 2008). The vertical, radial, and tangential components (*Z*, *R*, and *T*) are described in the following equations:

$$\begin{aligned} s_z = {} & M_{xx}\left[-\frac{\mathrm{ZSS}}{2}\cos(2\mathrm{az}) - \frac{\mathrm{ZDD}}{6} + \frac{\mathrm{ZEP}}{3}\right] \\ & + M_{yy}\left[-\frac{\mathrm{ZSS}}{2}\cos(2\mathrm{az}) - \frac{\mathrm{ZDD}}{6} + \frac{\mathrm{ZEP}}{3}\right] \\ & + M_{zz}\left[\frac{\mathrm{ZDD}}{3} + \frac{\mathrm{ZEP}}{3}\right] + M_{xy}[\mathrm{ZSS}\times\sin(2\mathrm{az})] \\ & + M_{xz}[\mathrm{ZDS}\times\cos(\mathrm{az})] + M_{yz}[\mathrm{ZDS}\times\sin(\mathrm{az})], \end{aligned} \tag{2}$$

$$\begin{aligned} s_r = {} & M_{xx}\left[\frac{\mathrm{RSS}}{2}\cos(2\mathrm{az}) - \frac{\mathrm{RDD}}{6} + \frac{\mathrm{REP}}{3}\right] \\ & + M_{yy}\left[-\frac{\mathrm{RSS}}{2}\cos(2\mathrm{az}) - \frac{\mathrm{RDD}}{6} + \frac{\mathrm{REP}}{3}\right] \\ & + M_{zz}\left[\frac{\mathrm{RDD}}{3} + \frac{\mathrm{REP}}{3}\right] + M_{xy}[\mathrm{RSS}\times\sin(2\mathrm{az})] \\ & + M_{xz}[\mathrm{RDS}\times\cos(\mathrm{az})] + M_{yz}[\mathrm{RDS}\times\sin(\mathrm{az})], \end{aligned} \tag{3}$$

$$\begin{aligned} s_r = {} & M_{xx}\left[\frac{\mathrm{TSS}}{2}\sin(2\mathrm{az})\right] + M_{yy}\left[-\frac{\mathrm{TSS}}{2}\sin(2\mathrm{az})\right] \\ & + M_{xy}[-\mathrm{TSS}\times\cos(2\mathrm{az})] + M_{xz}[\mathrm{TDS}\times\sin(\mathrm{az})] \\ & + M_{yz}[-\mathrm{TDS}\times\cos(\mathrm{az})], \end{aligned} \tag{4}$$

in which $s_z$, $s_r$, and $s_t$ are the vertical, radial, and tangential components of synthetic seismograms. $M_{xx}$, $M_{yy}$, $M_{zz}$, $M_{xy}$, $M_{xz}$, and $M_{yz}$ are the six independent components of the moment tensor, and az is the azimuth. *Z*DD, *Z*DS, *Z*SS, and *Z*EP are the vertical components of Green's function for the four basic source types; *R*DD, *R*DS, *R*SS, and *R*EP are the radial components; *T*DD, *T*DS, *T*SS, and *T*EP are the tangential components.

Following Zhu and Ben-Zion (2013), the gCAPjoint method replaces the full moment tensor with six parameters: moment magnitude ($M_w$), ISO-component parameter ($\zeta$ in the range of [−1,1]), CLVD-component parameter ($\chi$ in the range of [−0.5,0.5]), and fault geometry parameters corresponding to the DC components, that is, strike ($\phi_s$ in the range of [0,360°]), dip ($\delta$ in the range of [0,90°]), and rake ($\lambda$ in the range of [−180°,180°]) angles. These parameters are related to the moment tensor ($M_{ij}$) as follows (Zhu and Ben-Zion, 2013; Zhu and Zhou, 2016):

$$M_w = \log_{10}(1.5 \times M_0 + 16.1 - 7), \tag{5}$$

$$\zeta = \frac{\mathrm{trace}(M_{ij})}{\sqrt{6}M_0}, \tag{6}$$

$$\chi = \sqrt{\frac{3}{2}}\lambda_2, \tag{7}$$

$$M_0 = \sqrt{\frac{M_{ij}M_{ij}}{2}}, \tag{8}$$

$$M_{ij} = M_0\left[\sqrt{\frac{2}{3}} \times \zeta \times I_{ij} + \sqrt{1-\zeta^2} \times \left(\sqrt{1-\chi^2} \times \mathrm{DC}_{ij} + \chi \times \mathrm{CLVD}_{ij}\right)\right], \tag{9}$$

$$D_{ij} = \sqrt{1-\chi^2} \times \mathrm{DC}_{ij} + \chi \times \mathrm{CLVD}_{ij}, \tag{10}$$

$$\mathrm{DC}_{ij} = n_i v_j + n_j v_i, \tag{11}$$

$$\mathrm{CLVD}_{ij} = \frac{2b_i b_j - v_i v_j - n_i n_j}{\sqrt{3}}, \tag{12}$$

$$n_i = -\sin\delta\sin\phi_s \times \hat{x} + \sin\delta\cos\phi_s \times \hat{y} - \cos\delta \times \hat{z}, \tag{13}$$

$$v_i = (\cos\lambda\cos\phi_s + \cos\delta\sin\lambda\sin\phi_s) \times \hat{x} + (\cos\lambda\sin\phi_s - \cos\delta\sin\lambda\cos\phi_s) \times \hat{y} - (\sin\lambda\sin\delta) \times \hat{z}, \tag{14}$$

in which $i, j = 1, 2, 3$; $I_{ij}$ is the unit tensor, and $D_{ij}$ is a deviatoric tensor; $\lambda_2$ is the intermediate eigenvalue of the normalized deviatoric tensor; $n$ is the fault-normal vector, $v$ is the slip vector, $b = n \times v$ is the null vector; $\hat{x}, \hat{y}, \hat{z}$ are the Cartesian coordinates related to the north, east, and downward (Aki and Richards, 2002).

During waveform inversion, the local waveforms are segmented into *Pnl* waves on the vertical and radial components, and surface waves on the vertical, radial, and tangential components. The teleseismic waveforms include *P* on the vertical component and *SH* on the tangential component. The error function at each station is defined as the misfit between observed and synthetic waveforms aligned after cross-correlation. For seismic stations in sedimentary basins, short-period wave trains are sometimes quite long and may lead to the problem of cycle skipping. In this case, one could start the inversion via filtering seismic waveforms with a relatively long-period and restrict the time shift less than the half-cycle of the seismic waves. Then, the waveform inversion could be conducted with a shorter period and examine change of the time shift for different filtering band. In case of sudden change of the time shift, a cycle-skip might have occurred, and the time shift needs to be reinstated by removing the skipped cycles. The total error function is computed as the summation of the L2 norm of misfits for all stations,

$$Ec(h) = \sum_{i=1}^{n}\left[w_{\mathrm{loc}}\left(\frac{r_i}{r_0}\right)^p_{\mathrm{loc}} \times ||u_i - s_i||_{\mathrm{loc}} + w_{\mathrm{tel}} \times ||u_i - s_i||_{\mathrm{tel}}\right], \tag{15}$$

in which $Ec(h)$ is the total error for a given centroid depth of $h$, and $r$ is the local distance; $r_0$ is the reference epicentral distance for normalization purposes; $p$ is the factor to balance the weight of body and surface waves for different epicentral distances. Because the amplitudes of teleseismic body waves do not change rapidly with epicentral distance, the $p$ factor is fixed to be 1.0 for the teleseismic waveform fitting. $u_i$ is the observed waveform, and $s_i$ is the synthetic waveform at the $i$th station. Subscripts loc and tel refer to the local and teleseismic waveforms, respectively. As seismic waves at local distances are much stronger, the weight $\frac{w_{\mathrm{tel}}}{w_{\mathrm{loc}}}$ parameter is used to balance the effect of local and teleseismic data in the inversion. $||u_i - s_i||$ represents the L2 norm residuals between the observed and synthetic waveforms. Correlation coefficients can also be used to evaluate the match between observed and theoretical waveforms:

$$C(t) = \frac{\int_{t_1}^{t_2} s(\tau)u(t+\tau)d\tau}{[\int_{t_1}^{t_2} s^2(\tau)d\tau \int_{t_1}^{t_2} u^2(\tau)d\tau]^{1/2}}, \tag{16}$$

in which $t_1$ and $t_2$ stand for the time window for cross correlation. The window for teleseismic body waves can be

determined from travel-time calculations tools, such as TauP (Crotwell *et al.*, 1999).

The gCAPjoint algorithm uses the grid search method to obtain the focal depth, magnitude, focal mechanisms, and moment tensor. Grid interval of the strike, dip, and rake angle step is chosen to be 5°, and the magnitude is searched for with a step of 0.1, and the dimensionless parameter of ISO components is sampled for with a step of 0.1 as well as the CLVD components. Finer grid intervals can be chosen if more precise inversions are needed, but at the cost of longer inversion time.

## Example Application of gCAPjoint for Three Earthquakes

We verify the robustness of gCAPjoint using three moderately strong earthquakes occurred in various tectonic settings with different source depths. We tested the shallow 2017 Jiuzhaigou earthquake featuring dominant strike-slip mechanism along with non-DC components, the deeper 2010 Jiashian thrust earthquake also with some non-DC components, and the 2016 Pamir earthquake at depth about 200 km. Three-component broadband seismic waveforms of the earthquakes were requested from the Incorporated Research Institutions for Seismology (IRIS) or Data Management Centre of China National Seismic Network. After the removal of instrument responses, the seismic records are converted to ground particle velocity (cm/s) and then rotated to the great-circle path. Only seismic waveforms with high signal-to-noise ratio are retained for further processing.

### The 8 August 2017 $M_w$ 6.5 Jiuzhaigou earthquake

The Jiuzhaigou earthquake occurred in Sichuan province, China (Fig. 3a), and caused casualty and substantial economic losses. The earthquake caused 25 casualties and injured more than 500 people (Han *et al.*, 2018). After detailed modeling of Interferometric Synthetic Aperture Radar (InSAR) and teleseismic waveform data, Sun *et al.* (2018) proposed that this event occurred on multiple faults and featured obvious non-DC components. This earthquake is well recorded on many seismograph stations in local and global seismic networks (Fig. 3b), thus it is helpful for testing the gCAPjoint method.

The window lengths for the body and surface waves of Jiuzhaigou earthquake are chosen to be 60 and 80 s, respectively (Fig. 3c). Both the observed and synthetic waveforms are resampled to 5 samples per second. The corner frequencies of the band-pass filter are 0.02–0.1 Hz for *Pnl* and *P* waves, and 0.02–0.05 Hz for the surface and *SH* waves. The source duration was estimated with the scaling law (Somerville *et al.*, 1999), which is about 5.9 s. The passbands are chosen to avoid the strong noise of secondary microseism (~0.17 Hz) and to be low frequency enough to suppress 3D effects of small-scale crustal structures.

Source parameter solutions of this earthquake from various agencies are listed in Table 1. Most of the solutions show a similar magnitude between 6.4 and 6.5. The hypocentral depth from U.S. Geological Survey (USGS) is 9.0 km, while other agencies reported centroid depth greater than 13 km. In contrast, our study shows a much shallower centroid depth of 6 km in Figure 4, which is similar to the study based on InSAR and seismic waveforms (Sun *et al.*, 2018). The strong ground deformation observed with InSAR prefers shallow slips. As for the strike of the focal planes, our solution is consistent with others, which shows an error of less than 6°. However, the discrepancies between the dip and rake angles are relatively large. The maximum difference in dip and rake is up to 20° and 42°, respectively, that is, the USGS *W*-phase solution versus result by Han *et al.* (2018), and this could be an artifact, because Han *et al.* (2018) only invert for DC focal mechanisms. As for the non-DC components, Global CMT solution gave an estimate of 10%, USGS 20%, whereas our result revealed non-DC component up to 25%, following the definition of non-DC percentage by Dziewonski *et al.* (1981). Combining seismic waveform data and InSAR observation, the rupture model by Sun *et al.* (2018) confirmed clear non-DC components of this earthquake, which should be due to the rupture along three fault segments.

### The 4 March 2010 $M_w$ 6.2 Jiashian earthquake

The Jiashian earthquake occurred on 4 March 2010 in southern Taiwan (Fig. 5a). This earthquake was located at the Taiwan tectonic belt, which is an active arc-continental collision zone. Some studies suggest that this event probably occurred in the lower crust (Ching *et al.*, 2011; Hsu *et al.*, 2011). For example, the focal depth from Global CMT is 29.1 km.

In this study, we used waveform data similar to those in Chen *et al.* (2015) (Fig. 5a,b). The gCAPjoint inversion shows that the magnitude is $M_w$ 6.23 (Fig. 5c), the focal depth is 24.0 km, and the focal plane solution is as follows: nodal plane 1, strike 307°, dip 34°, and rake 44°; nodal plane 2, strike 178°, dip 67°, and rake 115°, close to focal plane solutions from other agencies (Table 2). The percentage of non-DC components from gCAPjoint is 14%, qualitatively consistent solutions by USGS (non-DC 17%) and Global CMT (non-DC 22%), which all show non-DC components. Lee *et al.* (2013) demonstrated substantial complexity of the rupture process along complex fault geometries, which might cause the appreciable non-DC components. Ching *et al.* (2011) utilized 139 consecutive Global Positioning System data to constrain the earthquake depth to be about 23 km, close to the results in this study.

### The 10 April 2016 $M_w$ 6.6 Pamir earthquake

On 10 April 2016, a moderately strong earthquake occurred at the western Pamir plateau. The available seismic stations are sparse near the earthquake (Fig. 6a). There are only three stations in the north and southwest direction, with a maximum azimuth gap of about 205°. Therefore, it is better to combine

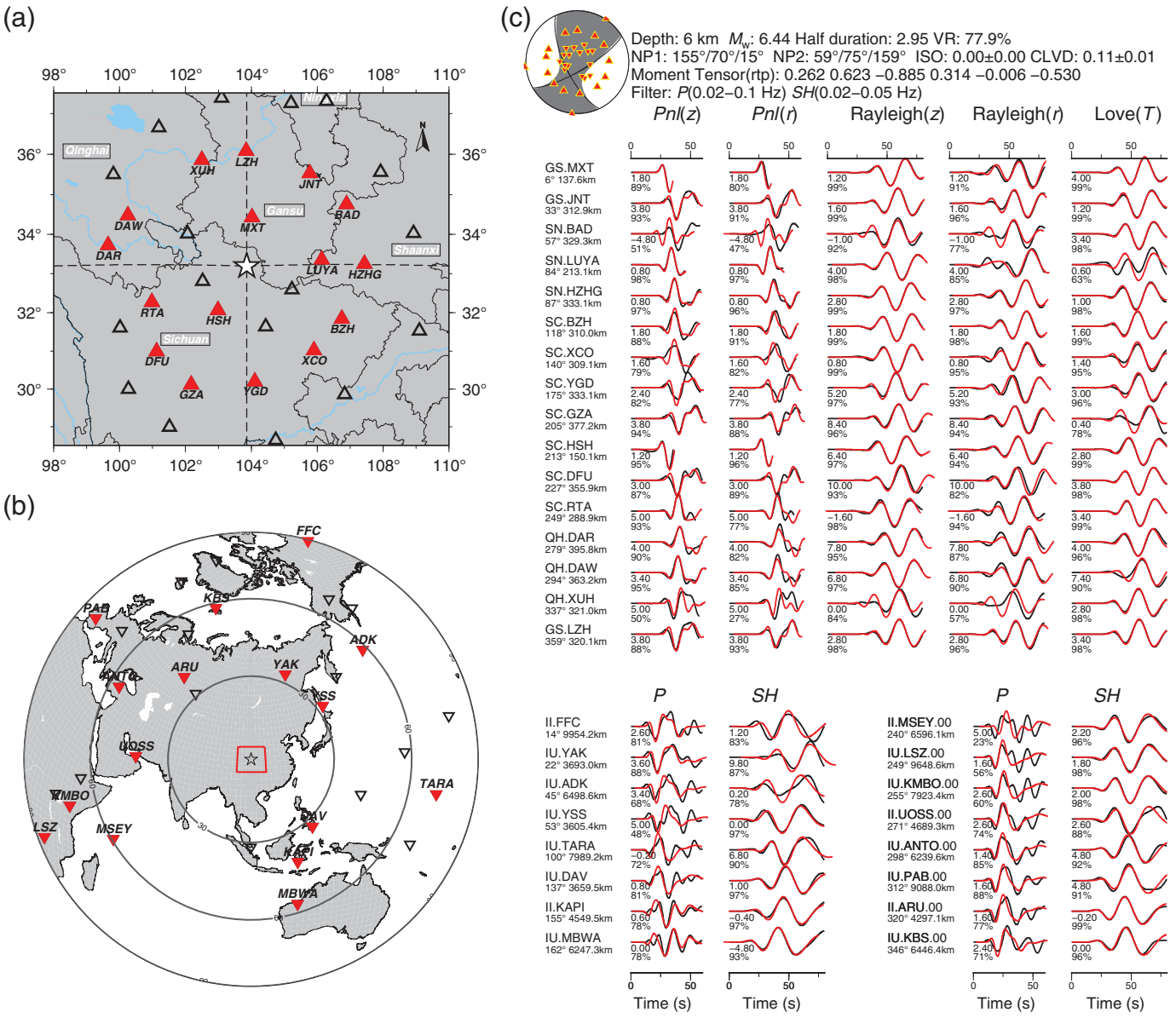


local and teleseismic waveform data to invert for the source parameters. As shown in Figure 6b, there are many teleseismic stations available for this earthquake.

Because there are only three local stations, we utilize them all in the dataset. We select 34 teleseismic stations to increase the sampling of the focal sphere (Fig. 6b). As this earthquake is deep, according to the USGS catalog in the Table 3, the window length of *Pnl* and *P* wavebands is chosen to be 150 s, and that of surface waves at local distance and *SH* waves at teleseismic distance is 200 s. On a Linux system work station (Intel Xeon CPU Core i7-8700K 3.70GHz), it takes about 308 s to perform inversion of earthquake source parameters, with 5° interval for searching focal plane angles (range of strike as 0°–360°, dip of 0°–90°, and rake of −180° to 180°). As for the depth, the interval is 1 km and the range is 160–260 km. The gCAPjoint inversion shows solution as follows: $M_w$ 6.59; centroid depth of 207 km; nodal plane 1, strike 274°, dip 37°, and rake 105°; nodal plane 2, strike 75°, dip 54°, and rake 78° (Fig. 6c). The percentage of non-DC components is 2% (Table 3), which means that it is dominated by the DC components (98%)

**Figure 3.** The gCAPjoint solution for the 2017 Jiuzhaigou earthquakes. (a) The earthquake (star) and local broadband stations (triangles). (b) Teleseismic broadband stations (inverted triangles). Black open triangles and inverted triangles indicate available stations, whereas red triangles and inverted triangles represent the stations actually used in inversion. (c) Summary of inversion at optimal depth. The black and red lines denote the observed and synthetic waveforms, respectively. Numbers to the left of the seismograms are time shifts (lower, first line numbers) and cross-correlation coefficient in percent (lower, second line numbers). Positive time shifts indicate that synthetic waveforms are delayed. The triangles on the focal sphere show the projection of *P* waves.

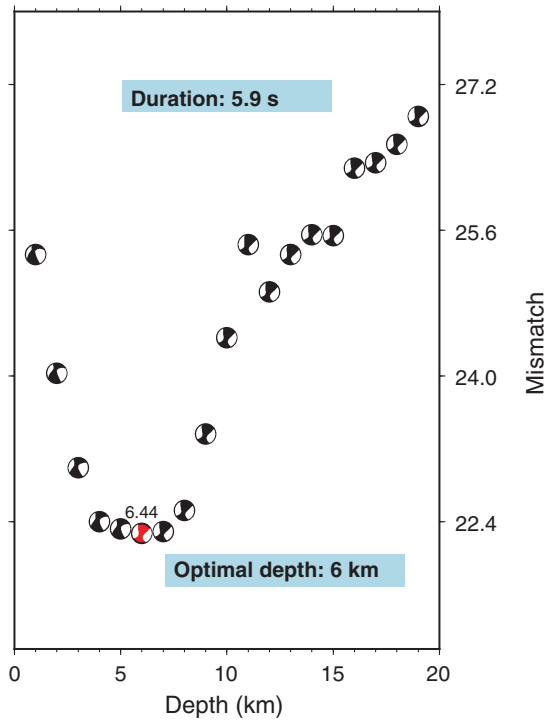


**Figure 4.** Waveform mismatch versus centroid depth for the 2017 Jiuzhaigou earthquakes. Red focal sphere indicates the focal mechanism at optimal depth.

consistent with the USGS and Global CMT catalogs. Considering the effect of error, it can be regarded as a relatively pure DC earthquake. This almost pure DC mechanism suggests that some intermediate-deep earthquakes might also occur on planar structures similar to fault planes in the shallow crust.

## Discussion

The gCAPjoint method takes advantage of local and teleseismic waveforms, which can provide better sampling of the focal sphere. Therefore, the joint inversion is sensitive to different source types of earthquakes, especially when local and teleseismic stations are sparse. To test the sensitivity of local and teleseismic waveforms in the gCAPjoint method, we take the 2017 Jiuzhaigou earthquake as an example. Previous inversions have shown that there are some non-DC components in the focal mechanism (Table 1). Here, we try to obtain focal mechanisms of this earthquake for the following five cases: (1) 16 local stations only, (2) 16 local and 4 teleseismic stations, (3) 16 local and 16 teleseismic stations, (4) 4 local and 16 teleseismic stations, and (5) 16 teleseismic stations only (Fig. 7a). The results show that the five focal mechanisms have similar DC components, but the non-DC components vary. For case 1 that only local waveforms are used, the center of the focal sphere is tensional. However, the center of the focal sphere is compressional for the results inverted with 16 local and 16 teleseismic waveforms (case 3). The focal mechanism of the case 3 is also

TABLE 1
**Source Parameters for the 2017 Jiuzhaigou Earthquake**

| Source | Moment Magnitude | Depth (km) | Planes I and II (Strike/Dip/Rake) (°) | Percent DC (%) |
|---|---|---|---|---|
| (USGS) PDE | 6.5 $M_{ww}$ | 9.0 | – | – |
| USGS *W*-phase | 6.5 $M_{ww}$ | 13.5 | 153/84/–33 | 79 |
| | | | 246/57/–173 | |
| USGS body wave | 6.4 $M_{wb}$ | 15.0 | 151/85/–4 | 90 |
| | | | 241/86/–175 | |
| Global CMT | 6.5 $M_w$ | 16.2 | 151/79/–8 | 93 |
| | | | 243/82/–168 | |
| CAP (Han *et al.*, 2018) | 6.5 $M_w$ | 14.0 | 156/65/9 | Assuming 100 |
| | | | 250/82/–154 | |
| gCAPloc | 6.44 $M_w$ | 6.0 | 152/69/–4 | 81 |
| | | | 244/86/–159 | |
| gCAPtel | 6.51 $M_w$ | 12.0 | 146/75/5 | 74 |
| | | | 55/85/165 | |
| gCAPjoint | 6.44 $M_w$ | 6.0 | 155/70/15 | 76 |
| | | | 59/75/159 | |

Origin time: 8 August 2017, 13:19:49; longitude: 103.855° E, latitude: 33.193° N. CAP, cut-and-paste method; DC, double couple; Global CMT, Global Centroid Moment Tensor; loc, local; PDE, Preliminary Determination of Epicenters; tel, teleseismic; USGS, U.S. Geological Survey.

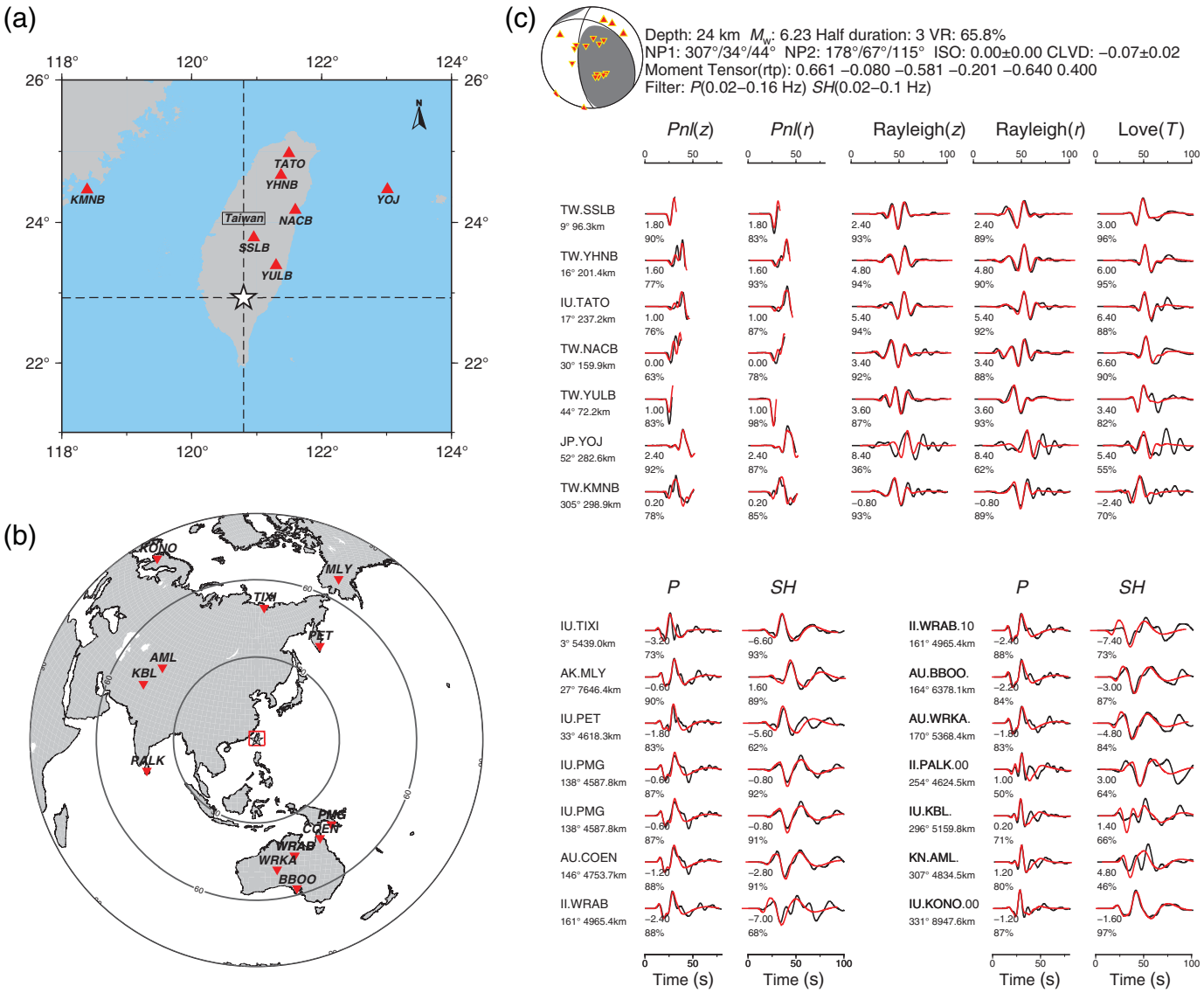


**Figure 5.** Waveform mismatch versus centroid depth for the 2010 Jiashian earthquake. Please refer to Figure 3 for more details.

different from the solutions of the Global CMT and *W*-phase inversions. The focal mechanisms of the five cases suggest that local waveform data only do not constrain the source mechanism well enough. Focal mechanisms of the Jiashian earthquake and the Pamir earthquake also demonstrate that the gCAPjoint method can be used to obtain source parameters of continental shallow earthquakes and intermediate-depth earthquakes effectively. For the intermediate-depth earthquakes, the gCAPjoint method not only improves the accuracy of the centroid depths, but also provides better constraints on focal mechanism solutions by more sampling areas of the focal sphere.

We obtained a centroid depth of 4 km using local waveforms only (case 1). For case 5, in which only teleseismic stations are involved, the centroid depth is about 12 km. The joint inversion with 16 local and 16 teleseismic waveforms shows a depth of 6 km (case 3). This discrepancy might be caused by several asperities of the earthquake, which are sampled by local and teleseismic waves with different sensitivities, thus leading to different centroid depths. Sun *et al.* (2018) presented a complex rupturing along three faults for the Jiuzhaigou earthquake. Zheng *et al.* (2019) studied the earthquake and proposed that there are two asperities, with one in the depth range between 2 and 12 km, with an average depth of 7 km. Then the earthquake rupture propagated along the N152°E direction and showed a second asperity in the depth range of 5 and 20 km. But there could be another reason for the discrepancy of depth from local and telseismic inversion. Usually, teleseismic body-wave data constrain focal depth better, because the teleseismic waveform includes the depth phases

TABLE 2
**Source Parameters for the 2010 Jiashian Earthquake**

| Source | Moment Magnitude | Depth (km) | Planes I and II (Strike/Dip/Rake) (°) | Percent DC (%) |
|---|---|---|---|---|
| (USGS) PDE | 6.3 $M_{wc}$ | 21.0 | – | – |
| USGS *W*-phase | 6.2 $M_{ww}$ | 35.0 | 310/26/42 | 83 |
| | | | 181/73/110 | |
| USGS body wave | 6.2 $M_{wb}$ | 21.0 | 325/32/47 | 73 |
| | | | 192/67/113 | |
| Global CMT | 6.3 $M_{wc}$ | 29.1 | 313/30/45 | 78 |
| | | | 183/69/112 | |
| CAPjoint Chen *et al.* (2012) | 6.17 $M_w$ | 21.0 | 317/36/52 | Assuming 100 |
| | | | 181/62/114 | |
| gCAPjoint | 6.23 $M_w$ | 24.0 | 307/34/44 | 86 |
| | | | 178/67/115 | |

Origin time: 4 March 2010, 00:18:51; longitude: 120.795° E, latitude: 22.918° N.

such as *pP*, *sP*, and so on. This is confirmed in the examples of 2010 $M_w$ 6.2 Jiashian (depth = 24 > 12 km) and 2016 $M_w$ 6.6 Pamir (depth = 207 > 12 km) earthquakes, especially the deep-focus earthquakes. However, for the Jiuzhaigou earthquake, it occurred with a shallow depth. Teleseismic wave inversion might suffer the problem of ambiguity between *sP* and *pP*, which are quite close to each other. In this case, surface waves are stronger, thus combination of local data and teleseismic data can improve the solution of depth.

The focal mechanisms of the five cases vary with relative weight between local and teleseismic waveforms. The amplitudes of the teleseismic waveforms are smaller than those of the local waveforms, due to longer propagation ray paths. It is necessary to introduce a parameter $\frac{w_{tel}}{w_{loc}}$ to balance the weight between local and teleseismic data in the gCAPjoint inversion (equation 15). To further test the effects of the weight parameter, we ran gCAPjoint for the case 3 with 16 local stations and 16 teleseismic stations using different $\frac{w_{tel}}{w_{loc}}$ (Fig. 7b,c). The results show that both focal mechanisms and centroid depths vary with the parameter $\frac{w_{tel}}{w_{loc}}$. Thus, we introduce a procedure to determine the weight parameter. Before the grid search, the weight parameter can be preliminarily set to 1. We then obtain the approximate equivalent weight parameter by the ratio of the misfits for the local-only fitting and teleseismic-only fitting. In general, a smaller number of local stations require a bigger weight of $\frac{w_{tel}}{w_{loc}}$ parameter. The weight parameter of the Jiuzhaigou earthquake is close to 30,000, as shown in Figure 7b, and the corresponding optimal centroid depth is 6 km (Fig. 7c).

The Global CMT and some other studies usually constrained the trace of moment tensor to be zero, which rules out the isotropic components (implosion or explosion source type). This assumption is applicable to most tectonic and crustal earthquakes, but occasionally there are events with isotropic components (Julian *et al.*, 1998; Templeton and Dreger, 2006). Our method is applicable to full moment tensor inversion, including the ISO and CLVD components grid searching in full parameter space. For deep-focus earthquakes, there are some controversies about the existence of non-DC components in deep-focus earthquakes. Shallow earthquakes may be affected by the 3D structures of crust and the fault complexity. However, for intermediate-deep and deep-focus earthquakes, some studies have observed significant CLVD components (Frohlich, 2006).

## Conclusion

We present the gCAPjoint package to jointly invert for source parameters, including full moment tensors and focal depth with local and teleseismic waveform data. This method can improve the accuracy of source parameters in area of sparse local seismic network. Robustness of the gCAPjoint package is assessed using three earthquakes with different depths and tectonic settings. The focal mechanism solution of the 2017 Jiuzhaigou earthquake shows substantial CLVD components, confirmed with tests of different numbers of local and teleseismic stations. The result is consistent with previous studies suggesting complex fault system and rupture history.

Current version of the gCAPjoint package uses one-dimensional velocity models to calculate synthetic waveforms. The gCAPjoint package can reduce the effects due to inaccurate velocity model through time shift. For most parts of the world, reliable 3D structure models of high precision

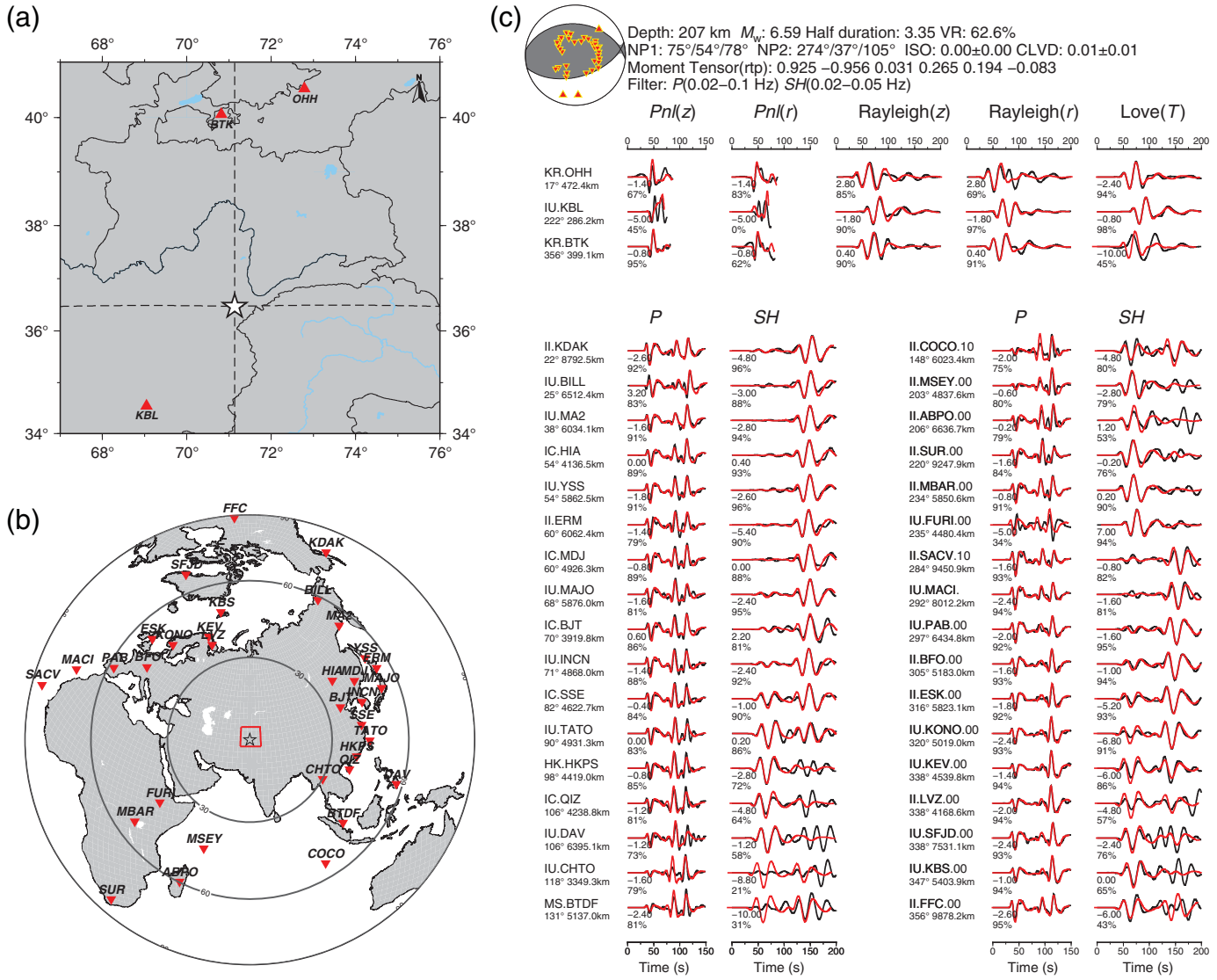


are unavailable, and the 1D velocity model is still routinely adopted for studies of earthquake sources. But with increasing resolution and reliability of seismic tomography, the gCAPjoint package can be straightforwardly ported for the case of Green's functions for 3D structures (Zhu and Zhou, 2016).

## Data and Resources

Seismic waveform data was requested from the Data Management Center of Incorporated Research Institutions for Seismology (IRIS) at http://ds.iris.edu/wilber3/find_event and the Data Management Centre of China National Seismic Network at Institute of Geophysics, China Earthquake Administration (SEISDMC, doi: 10.7914/SN/CB). Plotting of figures is based on the General Mapping Tools (http://www.soest.hawaii.edu/gmt/). The manual of generalized cut-and-paste joint (gCAPjoint) is provided in the supplemental material, and the software package is downloadable from https://www.github.com/bqpseismology/gCAPjoint. All websites were last accessed in August 2019.

**Figure 6.** Waveform mismatch versus centroid depth for the 2016 Pamir earthquake. Please refer to Figure 3 for more details.

## Acknowledgments

This study is supported by National Science Foundation of China (NSFC 41590854, 41874068). The authors acknowledge access to seismic waveform data of the following agencies: the Data Management Center of Incorporated Research Institutions for Seismology (IRIS), the Data Management Centre of China National Seismic Network at Institute of Geophysics, China Earthquake Administration (SEISDMC, doi: 10.7914/SN/CB). The authors also acknowledge the developers of the Generic Mapping Tools (GMT; Wessel and Luis, 2017) and thank Lupei Zhu for providing the generalized cut-and-paste (gCAP) package. The authors special thank the anonymous reviewers for suggestions and constructive comments on making this article more comprehensive.

TABLE 3
**Source Parameters for the 2016 Pamir Earthquake**

| Source | Moment Magnitude | Depth (km) | Planes I and II (Strike/Dip/Rake) (°) | Percent DC (%) |
|---|---|---|---|---|
| (USGS) PDE | 6.6 $M_{ww}$ | 212.0 | – | – |
| USGS *W*-phase | 6.6 $M_{ww}$ | 210.5 | 283/38/107 | 90 |
| | | | 82/54/77 | |
| USGS body wave | 6.7 $M_{wb}$ | 213.0 | 275/40/108 | 100 |
| | | | 72/53/76 | |
| Global CMT | 6.6 $M_{wc}$ | 210.8 | 278/38/106 | 92 |
| | | | 79/54/78 | |
| gCAPjoint | 6.59 $M_w$ | 207.0 | 274/37/105 | 98 |
| | | | 75/54/78 | |

Origin time: 10 April 2016, 10:28:58; longitude: 71.131° E, latitude: 36.473° N.

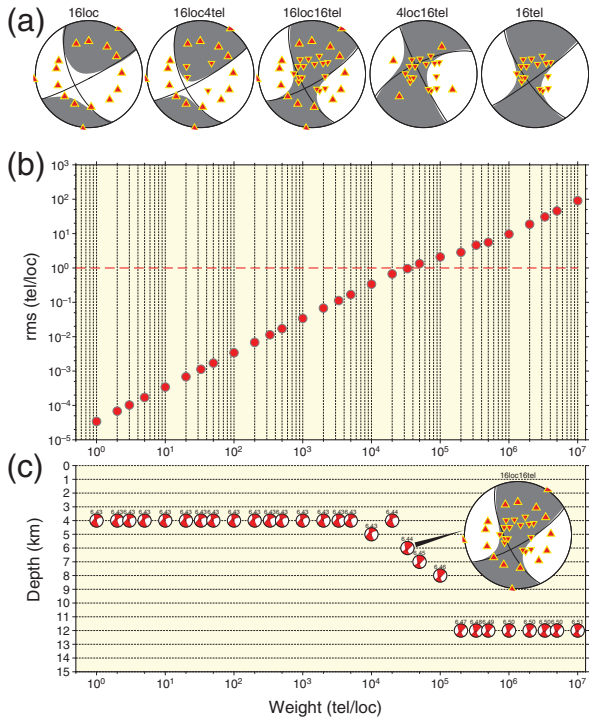


**Figure 7.** Tests on different number of local and teleseismic stations and $\frac{W_{tel}}{W_{loc}}$ weight factors. (a) Effects of different number of teleseismic and local stations. From left to right: 16 local stations only, 16 local and 4 teleseismic stations, 16 local and 16 teleseismic stations, 4 local and 16 teleseismic stations, 16 teleseismic stations only. (b) Root-mean-square (RMS) variation versus weight factors. The red dash line indicates the reference of weight factors ($\frac{W_{tel}}{W_{loc}} \approx 1$). (c) The optimal centroid depth and moment tensor solutions versus weight factors. The inset figure indicates the optimal focal mechanism and centroid depth inverted by 16 local and 16 teleseismic stations for the 2017 $M_w$ 6.5 Jiuzhaigou earthquake ($\frac{W_{tel}}{W_{loc}} \approx 1$).

## References


Adamova, P., E. Sokos, and J. Zahradnik (2009). Problematic non-double-couple mechanism of the 2002 Amfilochia $M_w$ 5 earthquake, Western Greece, *J. Seismol.* **13,** no. 1, 1–12, doi: 10.1007/s10950-008-9112-4.

Aki, K., and P. G. Richards (2002). *Quantitative Seismology*, Second Ed., University Science Books, Sausilito, California, ISBN: 0-935702-96-2.

Akinci, A., and L. Malagnini (2009). The 2009 Abruzzo earthquake, Italy, *IRIS Newsletter*, Issue 1.

Bassin, C. (2000). The current limits of resolution for surface wave tomography in North America, *Eos Trans. AGU* **81,** F897.

Baumbach, M., H. Grosser, H. Schmidt, A. Paulat, A. Rietbrock, C. R. Rao, P. S. Raju, D. Sarkar, and I. Mohan (1994). Study of foreshocks and aftershocks of the intraplate Latur earthquake of September 30, 1993, India, Latur Earthq. Memoir **35**, Geol. Soc. India, 33–63.

Cesca, S., E. Buforn, and T. Dahm (2006). Amplitude spectra moment tensor inversion of shallow earthquakes in Spain, *Geophys. J. Int.* **166,** no. 2, 839–854.

Chen, W., S. Ni, H. Kanamori, S. Wei, Z. Jia, and L. Zhu (2015). CAPjoint, a computer software package for joint inversion of moderate earthquake source parameters with local and teleseismic waveforms, *Seismol. Res. Lett.* **86,** no. 2A, 432–441.

Chen, W. W., S. D. Ni, Z. J. Wang, X. F. Zeng, and S. J. Wei (2012). Joint inversion with both local and teleseismic waveforms for source parameters of the 2010 Kaohsiung earthquake, *Chin. J. Geophys.* **55,** no. 7, 2319–2328 (in Chinese).

Ching, K.-E., K. M. Johnson, R.-J. Rau, R. Y. Chuang, L.-C. Kuo, and P.-L. Leu (2011). Inferred fault geometry and slip distribution of the 2010 Jiashian, Taiwan, earthquake is consistent with a thick-skinned deformation model, *Earth Planet. Sci. Lett.* **301,** nos. 1/2, 78–86.

Chu, R., S. Ni, A. Pitarka, and D. V. Helmberger (2014). Inversion of source parameters for moderate earthquakes using short-period teleseismic P waves, *Pure Appl. Geophys.* **171,** no. 7, 1329–1341, doi: 10.1007/s00024-013-0719-1.

Crotwell, H. P., T. J. Owens, and J. Ritsema (1999). The TauP Toolkit: Flexible seismic travel-time and ray-path utilities, *Seismol. Res. Lett.* **70,** 154–160.

D'Amico, S. (2018). *Moment Tensor Solutions*, Springer, Cham, Switzerland, ISBN: 978-3-319-77359-9.

Dreger, D. S., and D. V. Helmberger (1993). Determination of source parameters at regional distances with three-component sparse network data, *J. Geophys. Res.* **98,** no. B5, 8107–8125.

Dreger, D. S., and B. Woods (2002). Regional distance seismic moment tensors of nuclear explosions, *Tectonophysics* **356,** nos. 1/3, 139–156.

Duputel, Z., L. Rivera, H. Kanamori, and G. Hayes (2012). W phase source inversion for moderate to large earthquakes (1990–2010), *Geophys. J. Int.* **189,** no. 2, 1125–1147.

Dziewonski, A. M., and D. L. Anderson (1981). Preliminary reference Earth model, *Phys. Earth Planet. In.* **25,** no. 4, 297–356.

Dziewonski, A. M., T. A. Chou, and J. Woodhouse (1981). Determination of earthquake source parameters from waveform data for studies of global and regional seismicity, *J. Geophys. Res.* **86,** no. B4, 2825–2852.

Ekström, G., M. Nettles, and A. M. Dziewoński (2012). The global CMT project 2004–2010: Centroid-moment tensors for 13,017 earthquakes, *Phys. Earth Planet. In.* **200,** 1–9.

Ford, S. R., D. S. Dreger, and W. R. Walter (2008). Source characterization of the 6 August 2007 Crandall Canyon Mine seismic event in central Utah, *Seismol. Res. Lett.* **79,** no. 5, 637–644.

Frohlich, C. (1994). Earthquakes with non-double-couple mechanisms, *Science* **264,** no. 5160, 804–809.

Frohlich, C. (2006). *Deep earthquakes*, Cambridge University Press, New York, New York, ISBN: 0-521-92869-4.

Guilhem, A., L. Hutchings, D. S. Dreger, and L. R. Johnson (2014). Moment tensor inversions of M ∼ 3 earthquakes in the Geysers geothermal fields, California, *J. Geophys. Res.* **119,** 2121–2137.

Hamzehloo, H. (2005). Determination of causative fault parameters for some recent Iranian earthquakes using near field SH-wave data, *J. Asian Earth Sci.* **25,** no. 4, 621–628.

Han, L., J. Cheng, Y. An, L. Fang, C. Jiang, B. Chen, Z. Wu, J. Liu, X. Xu, and R. Liu (2018). Preliminary Report on the 8 August 2017 M s 7.0 Jiuzhaigou, Sichuan, China, earthquake, *Seismol. Res. Lett.* **89,** no. 2A, 557–569.

Herrmann, R. B., and C. J. Ammon (1997). Faulting parameters of earthquakes in the New Madrid, Missouri, region, *Eng. Geol.* **46,** nos. 3/4, 299–311.

Herrmann, R. B., L. Malagnini, and I. Munafò (2011). Regional moment tensors of the 2009 L'Aquila earthquake sequence, *Bull. Seismol. Soc. Am.* **101,** no. 3, 975–993.

Hsu, Y.-J., S.-B. Yu, L.-C. Kuo, Y.-C. Tsai, and H.-Y. Chen (2011). Coseismic deformation of the 2010 Jiashian, Taiwan earthquake and implications for fault activities in southwestern Taiwan, *Tectonophysics* **502,** nos. 3/4, 328–335.

Julian, B. R. (1983). Evidence for dyke intrusion earthquake mechanisms near Long Valley caldera, California, *Nature* **303,** no. 5915, 323–325.

Julian, B. R., and S. A. Sipkin (1985). Earthquake processes in the Long Valley caldera area, California, *J. Geophys. Res.* **90,** no. B13, 11,155–11,169.

Julian, B. R., A. D. Miller, and G. Foulger (1998). Non-double-couple earthquakes 1. Theory, *Rev. Geophys.* **36,** no. 4, 525–549.

Kanamori, H. (1993). W phase, *Geophys. Res. Lett.* **20,** no. 16, 1691–1694.

Kennett, B. (2005). Seismological tables: *ak135*, Produced by Research School of Earth Sciences, Australian National University, Canberra, Australia, 1–289.

Kennett, B., and E. Engdahl (1991). Traveltimes for global earthquake location and phase identification, *Geophys. J. Int.* **105,** no. 2, 429–465.

Kikuchi, M., and H. Kanamori (1982). Inversion of complex body waves, *Bull. Seismol. Soc. Am.* **72,** no. 2, 491–506.

Langston, C. A. (1978). The February 9, 1971 San Fernando earthquake: a study of source finiteness in teleseismic body waves, *Bull. Seismol. Soc. Am.* **68,** no. 1, 1–29.

Lee, S.-J., L. Mozziconacci, W.-T. Liang, Y.-J. Hsu, W.-G. Huang, and B.-S. Huang (2013). Source complexity of the 4 March 2010 Jiashian, Taiwan, earthquake determined by joint inversion of teleseismic and near field data, *J. Asian Earth Sci.* **64,** 14–26.

Li, J., G. Liu, X. Qiao, W. Xiong, X. Wang, D. Liu, J. Sun, A. Yushan, S. Yusan, W. Fang, and Q. Wang (2018). Rupture characteristics of the 25 November 2016 Aketao earthquake ($M_w$ 6.6) in eastern Pamir revealed by GPS and teleseismic data, *Pure Appl. Geophys.* **175,** no. 2, 573–585, doi: 10.1007/s00024-018-1798-9.

Li, Z., W. Feng, Z. Xu, P. Cross, and J. Zhang (2008). The 1998 $M_w$ 5.7 Zhangbei-Shangyi (China) earthquake revisited: A buried thrust fault revealed with interferometric synthetic aperture radar, *Geochem. Geophys. Geosyst.* **9,** no. 4.

Miller, A. D., G. R. Foulger, and B. R. Julian (1998). Non-double-couple earthquakes 2. Observations, *Rev. Geophys.* **36,** no. 4, 551–568.

Minson, S. E., and D. S. Dreger (2008). Stable inversions for complete moment tensors, *Geophys. J. Int.* **174,** no. 2, 585–592.

Sokos, E. N., and J. Zahradnik (2008). ISOLA a Fortran code and a Matlab GUI to perform multiple-point source inversion of seismic data, *Comput. Geosci.* **34,** no. 8, 967–977.

Somerville, P., K. Irikura, R. Graves, S. Sawada, D. Wald, N. Abrahamson, Y. Iwasaki, T. Kagawa, N. Smith, and A. Kowada (1999). Characterizing crustal earthquake slip models for the prediction of strong ground motion, *Seismol. Res. Lett.* **70,** no. 1, 59–80.

Sun, J., H. Yue, Z. Shen, L. Fang, Y. Zhan, and X. Sun (2018). The 2017 Jiuzhaigou earthquake: A complicated event occurred in a young fault system, *Geophys. Res. Lett.* **45,** no. 5, 2230–2240.

Tape, W., and C. Tape (2013). The classical model for moment tensors, *Geophys. J. Int.* **195,** no. 3, 1701–1720.

Templeton, D. C., and D. S. Dreger (2006). Non-double-couple earthquakes in the Long Valley volcanic region, *Bull. Seismol. Soc. Am.* **96,** no. 1, 69–79.

Vavryčuk, V., and D. Kühn (2012). Moment tensor inversion of waveforms: a two-step time-frequency approach, *Geophys. J. Int.* **190,** no. 3, 1761–1776.

Vavryčuk, V., M. Bohnhoff, Z. Jechumtálová, P. Kolář, and J. Šílený (2008). Non-double-couple mechanisms of microearthquakes induced during the 2000 injection experiment at the KTB site, Germany: A result of tensile faulting or anisotropy of a rock?, *Tectonophysics* **456,** no. 1, 74–93.

Wessel, P., and J. F. Luis (2017). The GMT/MATLAB Toolbox, *Geochem. Geophys. Geosyst.* **18,** no. 2, 811–823.

Zhao, L. S., and D. V. Helmberger (1991). Broadband modelling along a regional shield path, Harvard recording of the Saguenay earthquake, *Geophys. J. Int.* **105,** no. 2, 301–312.

Zheng, A. (2019). Study on the source rupture process of the complex seismogenic structure and the joint inversion of multiple types of data, *Ph.D. Dissertation*, University of Chinese Academy of Sciences, Beijing, China.

Zhu, L., and Y. Ben-Zion (2013). Parametrization of general seismic potency and moment tensors for source inversion of seismic waveform data, *Geophys. J. Int.* **194,** no. 2, 839–843.

Zhu, L., and L. A. Rivera (2002). A note on the dynamic and static displacements from a point source in multilayered media, *Geophys. J. Int.* **148,** no. 3, 619–627.

Zhu, L., and X. Zhou (2016). Seismic moment tensor inversion using 3D velocity model and its application to the 2013 Lushan earthquake sequence, *Phys. Chem. Earth. A* **95,** 10–18.

**Manuscript received 25 January 2020**
**Published online 19 August 2020**